

Ground deformation associated with post-mining activity at the French–German border revealed by novel InSAR time series method

Sergey Samsonov^{a,b,*}, Nicolas d'Oreye^{b,c}, Benoît Smets^b

^a Natural Resources Canada, 588 Booth Street, Ottawa, ON K1A 0Y7, Canada

^b European Center for Geodynamics and Seismology, Rue Josy Welter 19, L-7256 Walferdange, Luxembourg

^c National Museum of Natural History, Department of Geophysics/Astrophysics, Rue Josy Welter 19, L-7256 Walferdange, Luxembourg

ARTICLE INFO

Article history:

Received 20 September 2012

Received in revised form

17 December 2012

Accepted 18 December 2012

Keywords:

Synthetic Aperture Radar Interferometry
InSAR

SBAS

Time series analysis

Ground deformation

Ground subsidence

Greater Region of Luxembourg

Saarland

Lorraine

Mining and post-mining ground
deformation

ABSTRACT

We present a novel methodology for integration of multiple InSAR data sets for computation of two dimensional time series of ground deformation. The proposed approach allows combination of SAR data acquired with different acquisition parameters, temporal and spatial sampling and resolution, wavelength and polarization. Produced time series have combined coverage, improved temporal resolution and lower noise level. We apply this methodology for mapping coal mining related ground subsidence and uplift in the Greater Region of Luxembourg along the French–German border. For this we processed 167 Synthetic Aperture Radar ERS-1/2 and ENVISAT images acquired between 1995 and 2009 from one ascending (track 29) and one descending (track 337) tracks and created over five hundred interferograms that were used for time series analysis. Derived vertical and east–west linear deformation rates show with remarkable precision a region of localized ground deformation located above and caused by mining and post-mining activities. Time series of ground deformation display temporal variability: reversal from subsidence to uplift and acceleration of subsidence in the vertical component, and horizontal motion toward the center of the subsidence on the east–west component. InSAR results are validated by leveling measurements collected by the French Geological Survey (BRGM) during 2006–2008. We determined that deformation rate changes are mainly caused by water level variations in the mines. Due to higher temporal and spatial resolution the proposed space-borne method detected a larger number of subsidence and uplift areas in comparison to leveling measurements restricted to annual monitoring of benchmark points along roads. We also identified one deformation region that is not precisely located above the mining sites. Comparison of InSAR measurements with the water levels measured in the mining pits suggest that part of the water that filled the galleries after termination of the dewatering systems may come from this region. Providing that enough SAR data is available, this method opens new opportunities for detecting and locating man-made and natural ground deformation signals with high temporal resolution and precision.

Crown Copyright © 2012 Published by Elsevier B.V. All rights reserved.

1. Introduction

Synthetic Aperture Radar Interferometry (InSAR) is an established methodology for mapping ground deformation of natural (e.g. Schmidt et al., 2005; Beavan et al., 2010; Gonzalez et al., 2010; Chen et al., 2012; Zhao et al., 2012) and anthropogenic (e.g. Raucoales et al., 2003; Strozzi et al., 2011; Jiang et al., 2011; Zhang et al., 2012) causes. An interferogram is a conjugate product of two co-registered complex SAR images acquired by the same or similar sensor at two different times (Massonnet and Feigl, 1998; Rosen

et al., 2000). After removing Earth's curvature and topographic components, the InSAR image (also called differential interferogram) measures the ground deformation that occurred between image acquisitions but also signals related to travel time delays caused by water vapor in the troposphere and fluctuations of the electron content in the ionosphere (Hanssen and Feijt, 1996; Li et al., 2005). In a single differential interferogram deformation and atmospheric signals are indistinguishable, which limits accuracy and applicability of InSAR in case of small to moderate ground deformation (e.g. Gonzalez et al., 2010; Samsonov et al., 2010, 2011a).

The ability of InSAR to map ground deformation with sub-centimeter precision over a large area with only a fraction of the cost of ground based measurements has stimulated rapid progress in methodology development. One of the first studies that introduced InSAR applied to Earth Observation was of Massonnet

* Corresponding author at: Natural Resources Canada, 588 Booth Street, Ottawa, ON K1A 0Y7, Canada. Tel.: +1 613 9954913; fax: +1 613 9471385.

E-mail address: sergey.samsonov@nrcan-rcan.gc.ca (S. Samsonov).

et al. (1993), in which a single differential interferogram over southern California captured co-seismic displacements of the 1992 M7.3 Landers earthquake. A few years later Sandwell and Price (1998) introduced a stacking technique in which interferograms were combined into a single product with improved signal-to-noise ratio. A few years later Ferretti et al. (2001) introduced persistent scatterers (PS) methodology that extended applicability of InSAR to densely vegetated regions that were otherwise interferometrically incoherent. Finally Berardino et al. (2002) and Usai (2003) introduced Small Baseline Subset (SBAS) methodology that produces time series of ground deformation by computing a least-square solution from a large subset of interferograms and Hooper (2008) combined PS and SBAS techniques into a single methodology. Various modifications were also presented (e.g. Samsonov et al., 2011b; Hu et al., 2012), including those developed for studying 3D deformation (Rocca, 2003; Wright et al., 2004).

Fast progress in development of advanced InSAR methodologies was also caused by a steady increase in data quantities available for InSAR analysis. In the early 1990s the only operational SAR satellite was ERS-1 launched by the European Space Agency. By the early 2000s there were a few operational satellites (ERS-2, ENVISAT from ESA, RADARSAT-1 from CSA and ALOS from JAXA). Thanks to the generous data policy of ESA and other space agencies large sets of SAR data became widely accessible, promoting further development. A decade later, in the 2010s, multiple SAR satellites and satellite constellations (RADARSAT-2, Cosmo-SkyMed, TerraSAR-X) produce ever-growing quantities of data that demand further progress in methodology development for maximizing the effectiveness of interpretation.

At present the widely applied processing methodology is based on the SBAS technique. However, the standard SBAS when applied in a current environment has a few limitations: (i) it can only handle one InSAR data set at the time; (ii) it produces only the line-of-sight deformation time series, which are hard to interpret in case of complex signal; (iii) the produced time series have limited temporal coverage and coarse temporal resolution; (iv) due to poor temporal resolution the advanced filtering or/and regularization techniques have very limited applicability; consequently, (v) due to the poor temporal resolution and low signal-to-noise ration transient signals cannot be properly detected.

All these issues are automatically resolved in the proposed Multidimensional SBAS (MSBAS) method. If InSAR data from more than one orbital geometry is available MSBAS produces: (i) the multidimensional time series of ground deformation, in case of space-borne InSAR, vertical and horizontal east–west components; (ii) all InSAR data sets are utilized simultaneously, which allows to achieve uninterrupted temporal coverage and dense temporal resolution; (iii) dense temporal resolution allows the advanced processing, such as filtering and regularization, which improves signal-to-noise ratio and allows detection of the low-amplitude short-duration transient deformation.

In Samsonov and d'Oreye (2012) we demonstrated that over the past decade, hundreds of SAR images were collected over Virunga Volcanic Province (VVP, the Democratic Republic of Congo) from various satellites with different wave-length, resolution, acquisition geometry, and temporal sampling. These SAR images combined together produce over a thousand differential interferograms subdivided into eight SBAS time series (for each individual subset). VVP is not an exceptional region and even larger sets of data have been collected for many other areas including those selected as the research community supersites (<http://supersites.earthobservations.org/>). Manual analysis and interpretation of large sets of data consisting of hundreds to thousands of interferogram is clearly beyond human abilities and, therefore, new approaches are warranted.

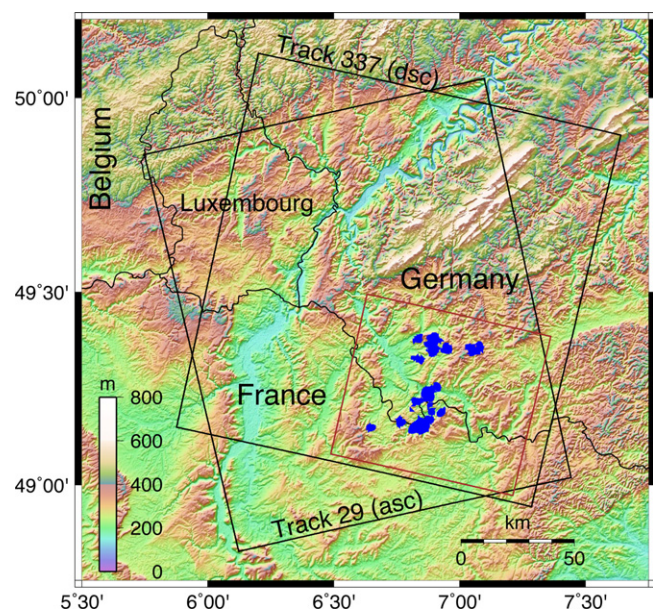


Fig. 1. Greater Region of Luxembourg. Country borders and ascending and descending ERS/ENVISAT frames are outlined in black. Region of interest is outlined in brown. Areas of fast subsidence (faster than -0.2 cm/year) are marked in blue.

In Samsonov and d'Oreye (2012) we provided in depth theoretical derivation of the MSBAS technique and performed error and sensitivity analysis in case of the non-negligible north–south component. We produced two dimensional time series of volcanic ground deformation derived from eight InSAR data sets over the highly coherent lava flow areas in the high altitude regions subjected to the significant tropospheric noise.

In this paper we apply a newly developed MSBAS methodology for mapping coal mining related ground subsidence and uplift in the low-coherent densely vegetated the Greater Region of Luxembourg along the French–German border (Fig. 1) and produce two dimensional time series of ground deformation derived from only two InSAR data sets. Historical leveling results reported in GIATM (2007) suggest that broader scale subsidence in this region started prior to 1961 (starting date of leveling campaigns). Rates of subsidence varied from a few mm/year to about 1 m/year but the area that experienced fastest subsidence according to leveling was only a few hundred m². The first InSAR results for this area were reported in Raucoules et al. (2007). The 1993–1993 ERS interferograms presented in Raucoules et al. (2007) had very limited coverage due to decorrelation, sufficient to identify presence of ground deformation but insufficient to measure the deformation rate precisely. The 1993–1994 JERS-1 interferograms showed localized areas with more than two fringes of LOS displacements (about 24 cm in total), however, such fast motion has not been confirmed by the ERS data nor the topographic error was evaluated, that could have been responsible for the observed fringes.

In this paper we combined over five hundred ERS-1/2 and ENVISAT interferograms from ascending and descending tracks to produce two components of the ground deformation with a remarkable precision. Ground deformation measured by our space-borne method is validated by comparison with the leveling measurements performed by the French Geological Survey (BRGM) during 2006–2008. Detected deformation rate changes are attributed to identified causes: termination of exploitation, termination of the dewatering operations and variation in the water levels in the abandoned galleries. At our resolution level we did not observe in our InSAR results any evidences of fast deformation but it cannot be excluded at the sub-resolution level. Using this

technique it is possible to reconstruct the complete 3D motion when data from at least three, including one non-near polar orbiting (e.g. air-borne), sensors becomes available.

2. Methodology

Our technique is based on the Small Baseline method (SBAS) proposed by Berardino et al. (2002) and Usai (2003) that was developed in order to reduce atmospheric contribution and decorrelation by computing a least square solution from many interferograms acquired under favorable conditions (e.g. small temporal and spatial baselines, absence of large atmospheric noise). One of the SBAS assumptions is that atmospheric noise is distributed randomly in time, therefore, a least-square solution calculated from many interferograms will reduce atmospheric signal, improving overall signal-to-noise ratio. This assumption may not hold in high elevation regions, where tropospheric stratigraphy is observed, but it is valid in most other regions.

The solution produced by SBAS is time series of line-of-sight (LOS) displacements for each pixel in a SAR image. For a single acquisition geometry, in the absence of additional information, the SBAS LOS solution cannot be decomposed into three components of the ground displacement vector (north, east, up) that would comprise a complete solution (e.g. Samsonov et al., 2007). However, if InSAR data from more than one acquisition geometry is available then SBAS methodology can be modified to produce an approximate solution consisting of time series of more than one component.

In the case of a single set of SAR images acquired by a sensor with an azimuth θ and an incidence angle ϕ the time series of deformation can be reconstructed by applying the following methodology:

$$AV_{los} = \Phi_{obs}, \quad V_{los} = A^+ \Phi_{obs}, \quad d_{los}^{i+1} = d_{los}^i + V_{los}^{i+1} \Delta t^{i+1}, \quad (1)$$

where A is a matrix constructed from the time intervals between consecutive SAR acquisitions, V_{los} is a vector of the unknown line-of-sight velocities, Φ_{obs} is a vector of observed interferogram values, A^+ is a pseudo-inverse of matrix A found by applying the Singular Value Decomposition (SVD), and d_{los}^i is a line-of-sight displacement at the time t^i .

In case of K multiple SAR sets acquired by sensors with different orbital parameters (e.g. azimuth and incidence angles) Eq. (1) can be rewritten in the following form for each set $k = 1, \dots, K$

$$|S_N^k A \quad S_E^k A \quad S_U^k A| \cdot |V_N \quad V_E \quad V_U|^T = \Phi_{obs}^k \quad (2)$$

assuming that $V_{los} = \mathbf{SV} = S_N V_N + S_E V_E + S_U V_U$ and $\mathbf{S} = \{S_N, S_E, S_U\} = \{\sin \theta \sin \phi, -\cos \theta \sin \phi, \cos \phi\}$, where \mathbf{S} is a line-of-sight unit vector with north, east and up components S_N , S_E , S_U , and \mathbf{V} is a velocity (ground deformation rate) vector with components V_N , V_E , V_U .

The generalized multidimensional SBAS method that includes all K sets of independently acquired SAR data can be presented in the following form

$$\begin{pmatrix} A^1 \\ A^2 \\ \dots \\ A^K \end{pmatrix} \times \begin{pmatrix} V_N \\ V_E \\ V_U \end{pmatrix} = \begin{pmatrix} \Phi^1 \\ \Phi^2 \\ \dots \\ \Phi^K \end{pmatrix} \quad \text{or} \quad \hat{A} \hat{V}_{los} = \hat{\Phi}_{obs} \quad (3)$$

where the new matrix \hat{A} has dimensions $3 \left(\sum_{k=1}^K N^k - 1 \right) \times \sum_{k=1}^K M^k$, the new vector \hat{V} has dimensions $1 \times 3 \left(\sum_{k=1}^K N^k - 1 \right)$, and the new vector $\hat{\Phi}_{obs}$ has dimensions $1 \times \sum_{k=1}^K M^k$.

This equation can be further simplified assuming that all modern space-borne SAR systems orbit the Earth in a near-polar orbit

and can acquire data only in two independent acquisition geometries: ascending and descending. Such acquisition geometries are insensitive to a motion in northern direction (i.e. along track) and, therefore, the number of unknowns in (3) can be reduced by excluding all terms responsible for northern motion V_N . The precision of this assumption was evaluated in Samsonov and d'Oreye (2012) where we showed that it does not significantly affect neither qualitative nor quantitative estimation of east–west and vertical deformation rates if the magnitude of north–south displacements is comparable to the magnitude of the two other components.

The described in (3) is a rank deficient problem that needs further justification. Indeed, rank deficiency is caused by the misalignment in acquisition times of the ascending and descending data sets. One of the obvious solutions to this problem is to interpolate both data sets on a common spatial grid. Such an approach solves the rank deficiency issue but introduces ambiguities in the selection of methodology for interpolation, common grid selection, and data redundancy. In Samsonov and d'Oreye (2012) we suggested two alternative approaches, temporal filtering and Tikhonov regularization (Tikhonov et al., 1998). Alternatively to Tikhonov regularization, truncated SVD (TSVD) methodology (Hansen, 1987) can also be implemented. It was demonstrated that even in case of significant atmospheric and computational (e.g. phase unwrapping, residual orbital ramps) noise, time series reconstructed with our methodology closely resemble the true deformation signal (Samsonov and d'Oreye, 2012). Such performance can be attributed to the Singular Value Decomposition applied to the ill-conditioned well-determined problem (Hansen, 1987), which is able to extract consistent information from a large set of noisy data. These qualities of SVD are well known and extensively used in other research areas, for example, data compression, noise reduction, and pattern reconstruction (e.g. Small, 1994; Hansen and Jensen, 1998).

3. Data processing

We performed interferometric processing of ERS and ENVISAT data (Table 1) independently and combined only final geocoded products. For each path and frame we selected a single master and co-registered all slave images to that master. All possible (5×20 multilooked) interferograms with perpendicular baseline less than 400 m and temporal baseline less than 1000 days were created. These threshold baseline parameters were chosen as a trade off between the number of interferograms and their quality measured by the interferometric coherence.

We further excluded interferograms calculated from ERS-2 images acquired after 2001 that were incoherent due to a large Doppler centroid variation caused by a failed gyroscope on the ERS-2 satellite. The topographic phase was removed using 90 m SRTM DEM data (Farr and Kobrick, 2000), interferograms were filtered, unwrapped using MCF algorithm (Costantini, 1998) and detrended by subtracting a fitted plane.

Small incoherent gaps in interferograms were filled by interpolation using maximum interpolation window radius 16 pixels and at least 16 coherent pixels. Interpolated interferograms were geocoded and re-sampled on 90 m \times 90 m grid. In the majority of the interferograms we did not observe any ground deformation signal above the noise level caused by severe decorrelation and tropospheric disturbances.

In total we produced 274 interferograms from 58 SAR images from the ascending track 29 and 311 interferogram from 113 SAR images from the descending track 337 (Table 1). These interferograms were used for the calculation of two dimensional time series using methodology (3). For this we initially performed a run in which we assumed that the average displacement for each

Table 1

SAR data sets used in this work: time span (in YYYYMMDD format), azimuth θ and incidence ϕ angles, number of available SAR images N , and number of calculated interferograms M .

InSAR set	Time span	θ ($^{\circ}$)	ϕ ($^{\circ}$)	N	M
ERS/ENVISAT, Track 29 (asc)	19930418–20110202	-16	23	59	274
ERS/ENVISAT, Track 337 (dsc)	19950713–20090326	-161	23	113	311
Total (only used images)	19950713–20090326			167	585

interferogram is zero. This run produced a linear deformation map similar to one shown in Fig. 2 that identified stable regions and regions of fast deformation. For the second run we selected five small stable regions as a reference and we calibrated each interferogram assuming that the average deformation at the chosen reference regions is zero. We produced two dimensional time

series for each pixel and calculated vertical and east–west linear deformation rates using linear regression analysis. Significant ground deformation was observed only in the SE corner of the studied region presented in Fig. 2 and our further discussion is limited to that region (area outlined in brown in Fig. 1).

The vertical and east–west components of deformation for twenty actively deforming regions are shown in Fig. 2 and the time series are plotted in Fig. 3. In order to improve signal-to-noise ratio and the quality of visualization in Fig. 3 we performed an additional averaging of pixels in a 15×15 window. Due to interpolation (i.e. low-pass filtering) and prior multi-looking it is expected that small regions of extreme deformation are over-smoothed. This, for example, can be seen in the subplot shown in Fig. 2(a) (in bottom-right). Here we plotted the line-of-sight linear deformation rate calculated from 26 highly coherent interferograms spanning 1996–2000 from the descending track 337. A subsidence with a rate about -4 cm/year is observed at two smaller regions located near point 1. By comparing this results with two dimensional time series shown in Fig. 3(a) it is apparent that part of the motion was attributed to a horizontal westward displacement that partially compensated a vertical displacement (in descending geometry). No evidence of motion faster than -4 cm/year suggested in Raucoules et al. (2007) was detected on any interferograms.

The fastest subsidence is observed at points 1 and 9 reaching approximately -1 cm/year over the 1994–2010 observation period. Vertical time series at points 1–8 show remarkable reversals from subsidence to uplift that started in 2006–2007 until the end of the observation period. Subsidence at other regions continues until the end of the observation period and subsidence at point 15 accelerates after 2006.

East–west time series show temporal variability on the order of 1 cm over the observation period. Clear horizontal motion toward the center of the subsidence is observed at some regions. For example, points 10, 15, 19, located on the western slope of the subsidence bowl experience eastward motion toward the center of subsidence and points 11, 12, 14, 20, located on the eastern slope of the subsidence bowl experience westward motion.

Identified deformation are further analyzed and validated by comparison with ground based leveling measurements.

4. Results and validation

Mining activity in this region started in the 18th Century and it continues today. Each mining site, contoured in black in Fig. 4 based on the 1:25,000 map from Charbonnages de France (GIATM, 2007) is composed of various levels of galleries. They are located at depths ranging from a few meters to more than 1000 m at the deepest sites. These mining sites are interconnected with networks of additional galleries and pits for water drainage, maintenance, extraction and air circulation, forming large interconnected clusters.

Linear deformation maps (Fig. 2) calculated with InSAR are compared to the spatial location and extent of the mining sites (Fig. 4). Clearly, all subsidence takes place above the mining sites. These deformation are well known as they reached several meters in some areas during the period of intense exploitation, causing

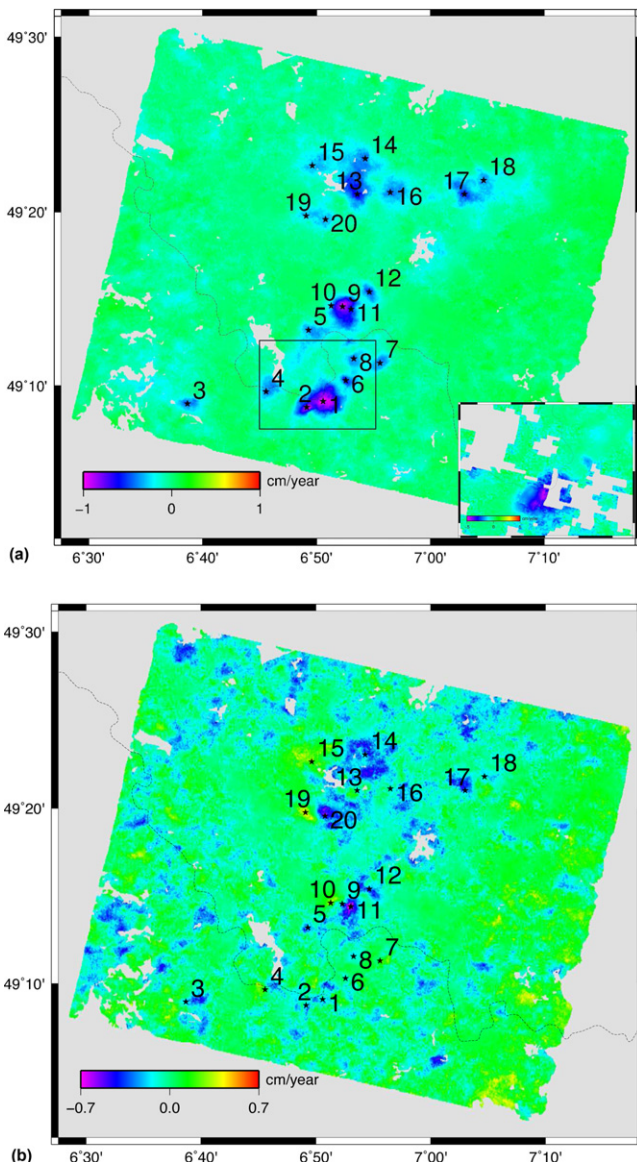


Fig. 2. Vertical (top) and east–west, (bottom) linear deformation rates (in cm/year) calculated by fitting line to time series calculated by proposed technique. Ground subsidence caused by mining activities is clearly visible on vertical deformation map. Horizontal displacements toward center of subsidence are also observed at some locations. For points 1–20 we present below time series of deformation. For area outlined by black rectangle in (a) we show SBAS LOS linear deformation rate calculated from 26 highly coherent interferograms spanning 1996–2000 from descending track 337 (color scale ranges from -5 to 5 cm/year).

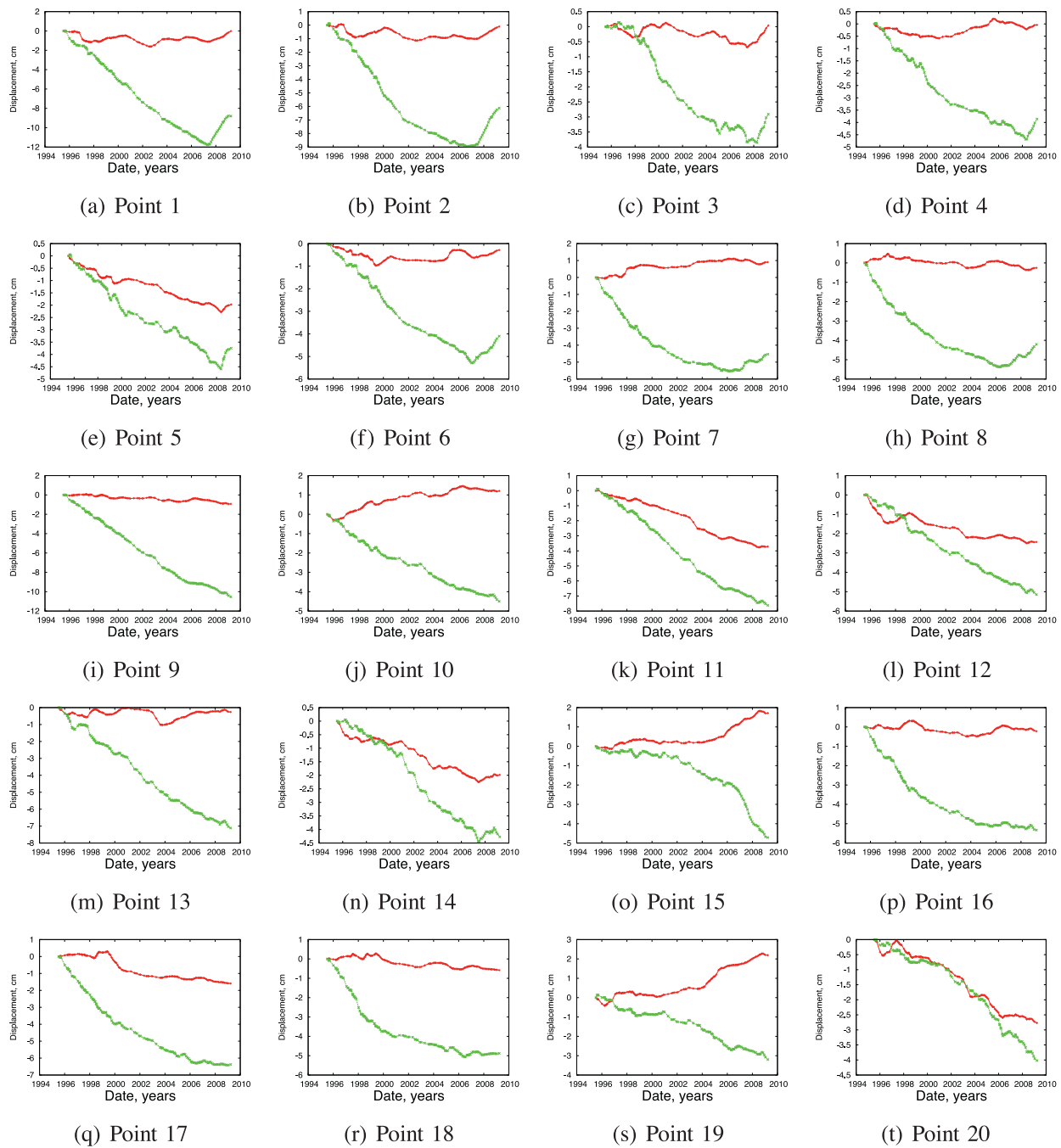


Fig. 3. Time series of ground deformation for 15×15 pixel regions 1–20 shown in Fig. 2 calculated by proposed technique. Vertical (green) and horizontal east–west (red) time series are shown.

extensive damage to houses and infrastructure (<http://www.lorraine.developpement-durable.gouv.fr/risques-miniers-et-sous-sols-r1560.html>). Since the progressive closure of the mining operations, the rate of deformation at some sites has decreased and even reversed to uplift.

By looking at the twenty time series presented in Fig. 3, it is apparent that all points located in France (points 1–4 and points 6–8) are affected by a reversal from subsidence to uplift, while all points in Germany, except point 5, do not show any reversal. Such reversal is typically linked to the end of exploitation, when water drainage stops and galleries are progressively flooded (Blachowski et al., 2009; Didier et al., 2008).

In the present case the last exploitation stopped at La Houve in Lorraine (French side) at the end of 2004 and flooding started

in June 2006 (DREAL, 2008, 2009). In contrast, mining in Germany remains active in the Sarre region. As the French and German mining networks are interconnected, a dam was built to separate the galleries to prevent the flooding from progressing to the German side. A 70 bar resistant plug was built in 2006 in a gallery at 1100 m depth (GIATM, 2006), W-SW of Gersweiler in Germany (see red bar in box C-E of Fig. 4). Consequently, point 5, located within the German mining sector but outside of the area protected by the dam remained connected to the French network, was also flooded (BRGM, 2009).

As the ground deformation is known to continue after termination of the exploitation, they remain under careful scrutiny by local authorities. The French geological survey (BRGM) performs intensive leveling campaigns. Nearly seventeen hundred

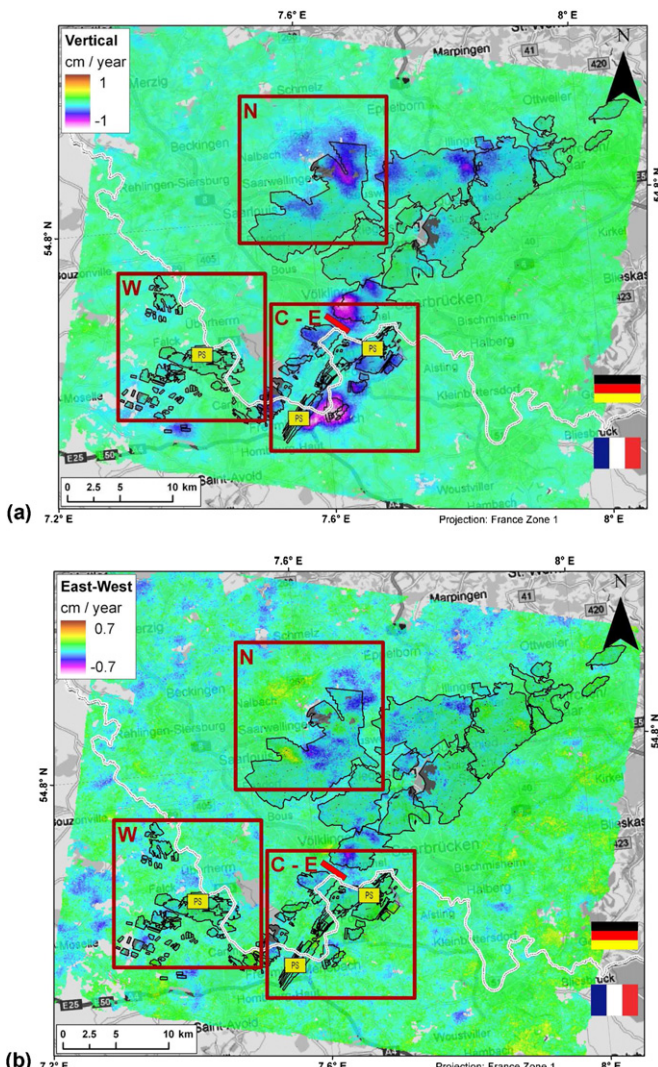


Fig. 4. Vertical (top) and east-west (bottom) linear deformation rates as in Fig. 2 with mining sites outlined in black (filled with light gray). Deformation clearly occur above mining sites. Outlined in red are “Western”, “Central an Eastern” and “Northern” sectors studied in more details in Figs. 5–8. Pumping stations tagged PS are former mining pits where water level is measured. From left to right: La Houve, Vouters and Simon pits. Small red bar locates 70 bar dam built at 1100 m depth.

leveling benchmarks located along roads and paths are measured annually. Vertical displacements are measured with an uncertainty better than 2 cm and contour maps are estimated (DREAL, 2009). Horizontal displacements are monitored by leveling only along 10 benchmarks close to E4 (Fig. 5) and 55 benchmarks in the region of the strongest (-10 cm) subsidence near C4 (Fig. 5) (BRGM, 2009) but this data is unfortunately unavailable. We used leveling measurements performed between 2006 and 2008 for validation of deformation detected with our method. Some regions of deformation reported by BRGM are only a few hundreds of meters wide. For this reason we compare leveling results with single pixel ($90\text{ m} \times 90\text{ m}$) time series instead of the 15×15 pixels ($1350\text{ m} \times 1350\text{ m}$) average shown in Fig. 3.

Three sectors (red boxes in Fig. 4) are studied in more detail. Ground deformation is compared to the water levels measured in nearby pits (BRGM, 2009): Simon, Vouters and La Houve pits in France (Fig. 4), and Geislautern and Ludweiler pits in Germany (not located on the map). Observed ground deformation and the water level variations show unquestionable similarities. Mechanisms that cause uplift after flooding however, are not clear and may be of

various sources: unloading due to water level rise, pore pressure variations, swelling of soil or materials at depth, etc. As we do not have detailed maps of the mining sites and we do not know the link between the pumping stations and the galleries from each mining site nor the depths of galleries, we do not intend to conduct a qualitative study of the water–ground deformation interactions. Nevertheless, the correlations observed at various scales (in time and space) allow us to validate the new InSAR method and propose new opportunities for high resolution ground deformation monitoring.

4.1. Ground deformation in the “Eastern and Central” sector

The “Eastern and Central” sector (using French administration naming convention) includes French communes Merlebach, Rosbruck, Morsbach, Forbach, Petite-Roselle and Stiring-Wendel and the German commune GrossRosseln (Figs. 5 and 6). Vouters and Simon pits are located respectively in the “Central” and “Eastern” sector. Both are close to German Geislautern and Ludweiler pits.

For the “Eastern” sector the June 2006–June 2008 leveling contour maps from BRGM display three distinct patches of -2 cm subsidence (green polygons in Fig. 5(a)). On the opposite, InSAR (Fig. 5(b)) detects a broader scale uplift mapped representatively at points E1 (0.7 cm), E2 (0.6 cm), E3 (0.1 cm) and E5 (0.4 cm), and only point E4 experiences subsidence of -0.2 cm (Fig. 5(c)–(g)).

Sub-centimeter uplift at points E1 and E2 is probably too small to be detected by leveling with a reported precision of about 2 cm . Clear correlation can be observed between the water level measured at Simon pit (dark blue curve in Fig. 5(c) and (d)), possibly with a combined effect of flooding at other mining sites, for example, the water level measured at Geislautern pit (in pink). In particular, after the reversal from subsidence to uplift initiated by the start of flooding marked by dashed line (3), the uplift stopped for a few months as the water level rise was suspended by pumping from the second half of 2007 up to early 2008. Such a step-like behavior is also visible on the time series from points E3 and E5 (Fig. 5(e)–(g)), although with a much lower amplitude. Although the InSAR time series seem once again consistent with water level fluctuations, the displacements observed for points E3–E5 disagree with the leveling results that contour very localized and narrow -2 cm subsiding areas. We believe that discrepancy observed at these narrow $50\text{--}300\text{ m}$ wide areas of subsidence can be attributed to the following possible causes: (i) over-smoothing of InSAR data during multilooking and geocoding to 90 m resolution and filtering applied during InSAR processing; (ii) InSAR phase aliasing during phase unwrapping caused by the fast deformation gradient and insufficient spatial sampling; (iii) inaccurate dating of leveling campaigns available to us; (iv) mismatch in referencing of InSAR and leveling measurements. Since the signal reverts from subsidence to uplift during the considered time span, a small imprecision in the time may lead to significant different inferred gradient, or even to a movement in the opposite direction (see also how this is well illustrated for point C4 here below).

Moreover, the time series from point E4 (Fig. 5(f)) also disagree with the leveling results and do not show similarities with the water level fluctuations. Point E4 is located in the narrow elongated contour drawn by BRGM which is actually along a road overhanging a high and steep quarry cliff. We believe that displacements at this point measured by leveling are actually related to a very localized phenomenon possibly affecting the road.

The moderate uplift measured by InSAR in the “Eastern” sector seems to be in agreement with a larger scale uplift measured by InSAR and leveling in the “Central” sector. The June 2006–December 2008 “Central” sector leveling contour maps from BRGM (Fig. 6(a)) display three regions of uplift (in orange) and one region of subsidence (in green). In this map light-to-dark green polygons

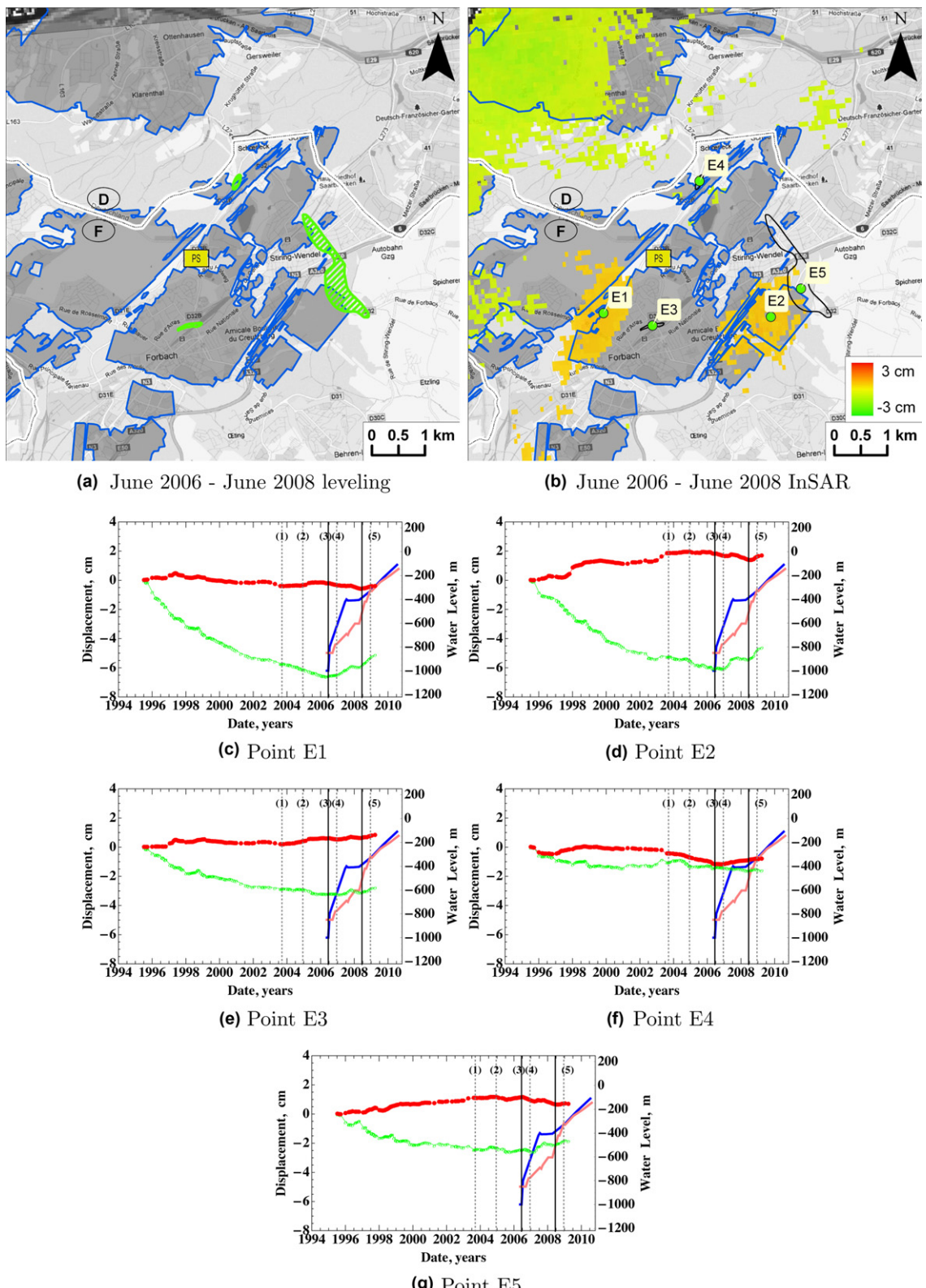


Fig. 5. (a) Ground deformation measured by leveling performed by BRGM between June 2006 and December 2008 in “Eastern” sector. Polygons correspond to 2 cm (orange), –2 cm (light green) and –10 cm (dark green) of vertical displacements. Mining sites are outlined in blue. French–German border is shown as white and black line. (b) Deformation measured by InSAR between between June 2006 and December 2008. Contours of BRGM leveling results are outlined in black for comparison. Green dots mark E1–E5, locations of pixels for which time series are shown. PS is pumping station “Simon 5” in former mining pit where water level is measured. (c–g) Time series of vertical (green) and east–west (red) displacements measured by proposed technique during 1995–2009 at points E1–E5. Vertical dashed lines numbered (1) and (2) mark respectively termination of exploitation in Merlebach and La Houve sectors. Dashed lines (3) and (4) mark beginning of flooding of mines in “Eastern and Central” and “Western” sectors respectively. Dashed line (5) marks end of flooding in “Western” sector (BRGM, 2009). Vertical solid lines, superimposed on lines (3) and (5), delimit time span of the BRGM leveling campaigns used for comparison in panels (a) and (b). Water levels measured in nearest pits are shown for comparison: “Simon” (blue) in France and “Geislautern” (pink) in Germany.

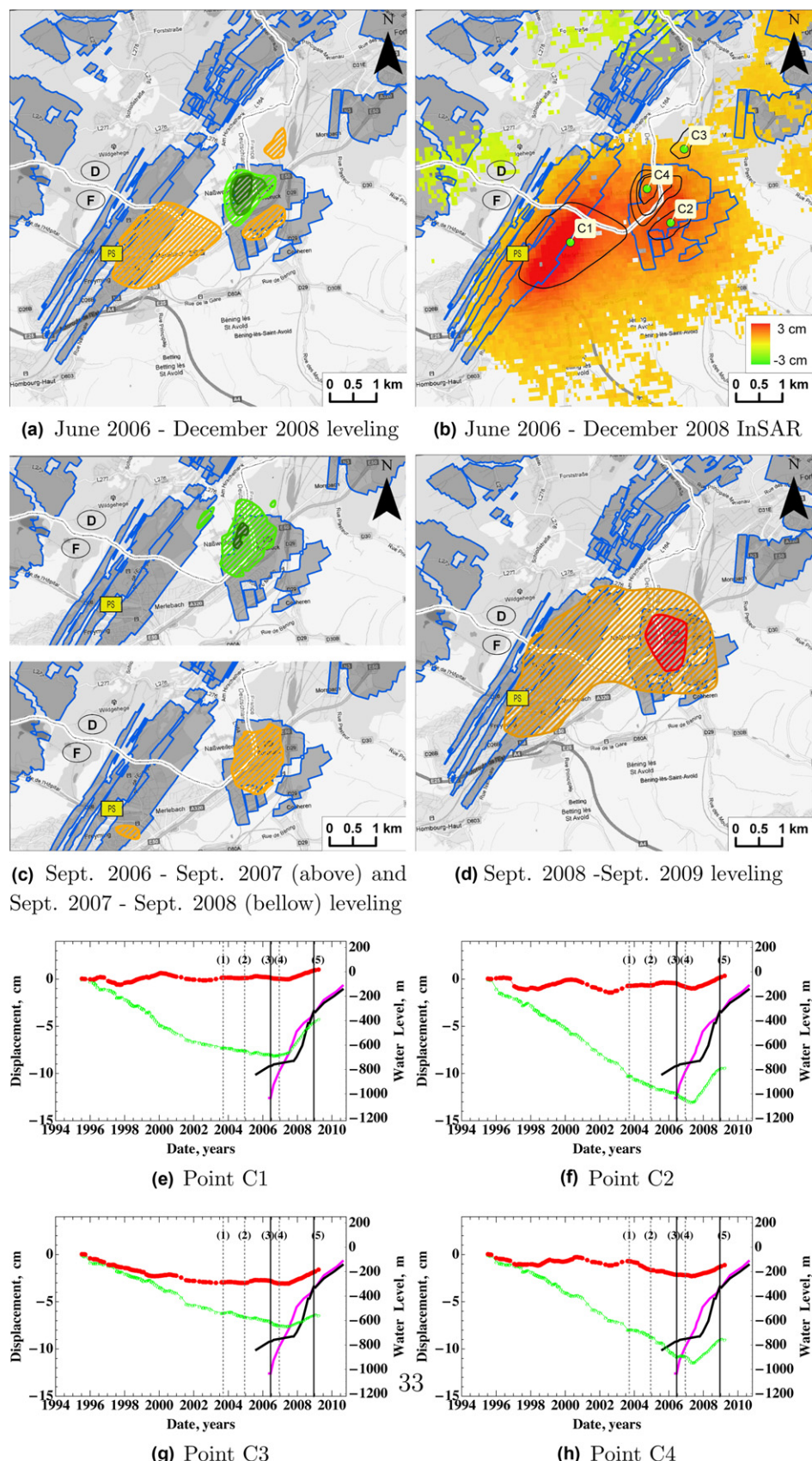


Fig. 6. Ground deformation measured by leveling performed by BRGM between (a) June 2006 and June 2008, (c, above) September 2006 and September 2007, (c, below) September 2007 and September 2008, and (d) September 2008 and September 2009 in “Central” sector. (b) Deformation measured by InSAR between June 2006 and December 2008. Green dots mark C1–C5, locations of pixels for which time series are shown. PS is pumping station “Vouters” in former mining pit where water level is measured. (e–h). Time series of vertical (green) and east–west (red) displacements measured by proposed technique during 1995–2009 at points C1–C4. Water levels measured in nearest pits are shown for comparison: “Vouters” (magenta) in France and “Ludweiler” (black) in Germany. Scale, polygon colors, outlines and vertical lines are as in Fig. 5.

depict subsidence from -2 to -10 cm and orange polygons depict uplift of 2 cm. It is interesting that BRGM leveling maps spanning September 2006–September 2007 (Fig. 6(c), above) and September 2007–September 2008 (Fig. 6(c), below) show signals of opposite direction that do not sum to the combined signal shown in the 2006–2008 map (Fig. 6(a)). During the same time InSAR measurements show a clear uplift that started from the middle of 2007 (associated with the termination of water pumping) and continues until the present time (Fig. 6(b)). In this map light-to-dark green

polygons depict subsidence ranging from -0.5 cm up to -4 cm and orange-to-red polygons depict uplift of 0.5 cm to 4 cm. Smaller deformation (between -0.5 cm and 0.5 cm) are omitted for clarity. In addition, the overall pattern of deformation reported by InSAR for that period is more consistent (both in shape and amplitude) with the reported leveling from September 2008–September 2009 (Fig. 6(d)), which confirms that discrepancies between leveling and InSAR might be mainly due to inaccurate dating of leveling campaigns available to us.

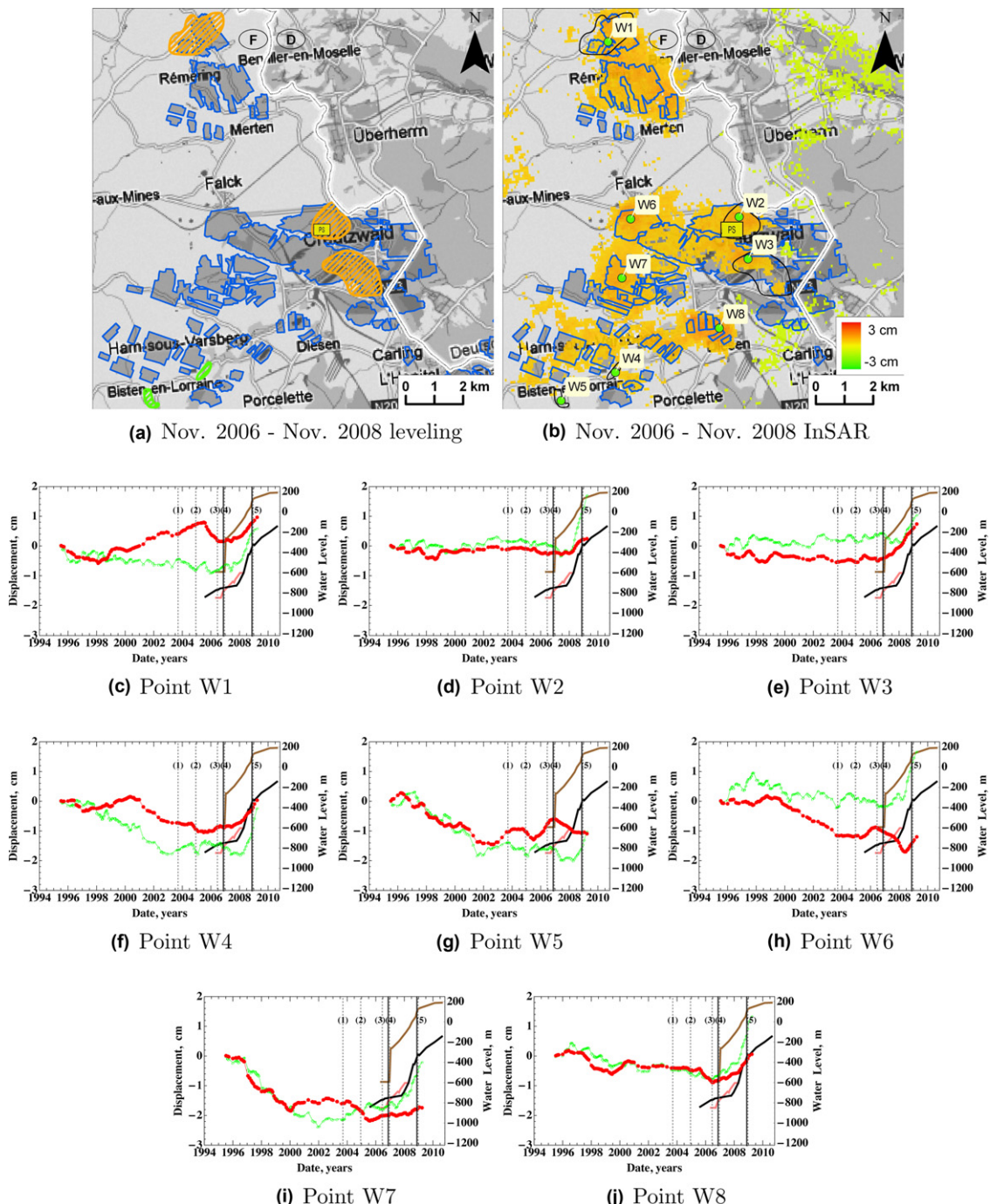


Fig. 7. (a) Ground deformation measured by leveling performed by BRGM between November 2006 and November 2008 in "Western" sector. (b) Deformation measured by InSAR between November 2006 and November 2008. Green dots mark W1–W8, locations of pixels for which time series are shown. PS is pumping station "La Houves" in former mining pit where water level is measured. (c–j) Time series of vertical (green) and east–west (red) displacements measured by proposed technique during 1995–2009 at points W1–W8. Water levels measured in nearest pits are shown for comparison: "La Houves" (brown) in France and "Geislautern" (pink) and "Ludweiler" (black) in Germany. Scale, polygon colors, outlines and vertical lines are as in Fig. 5.

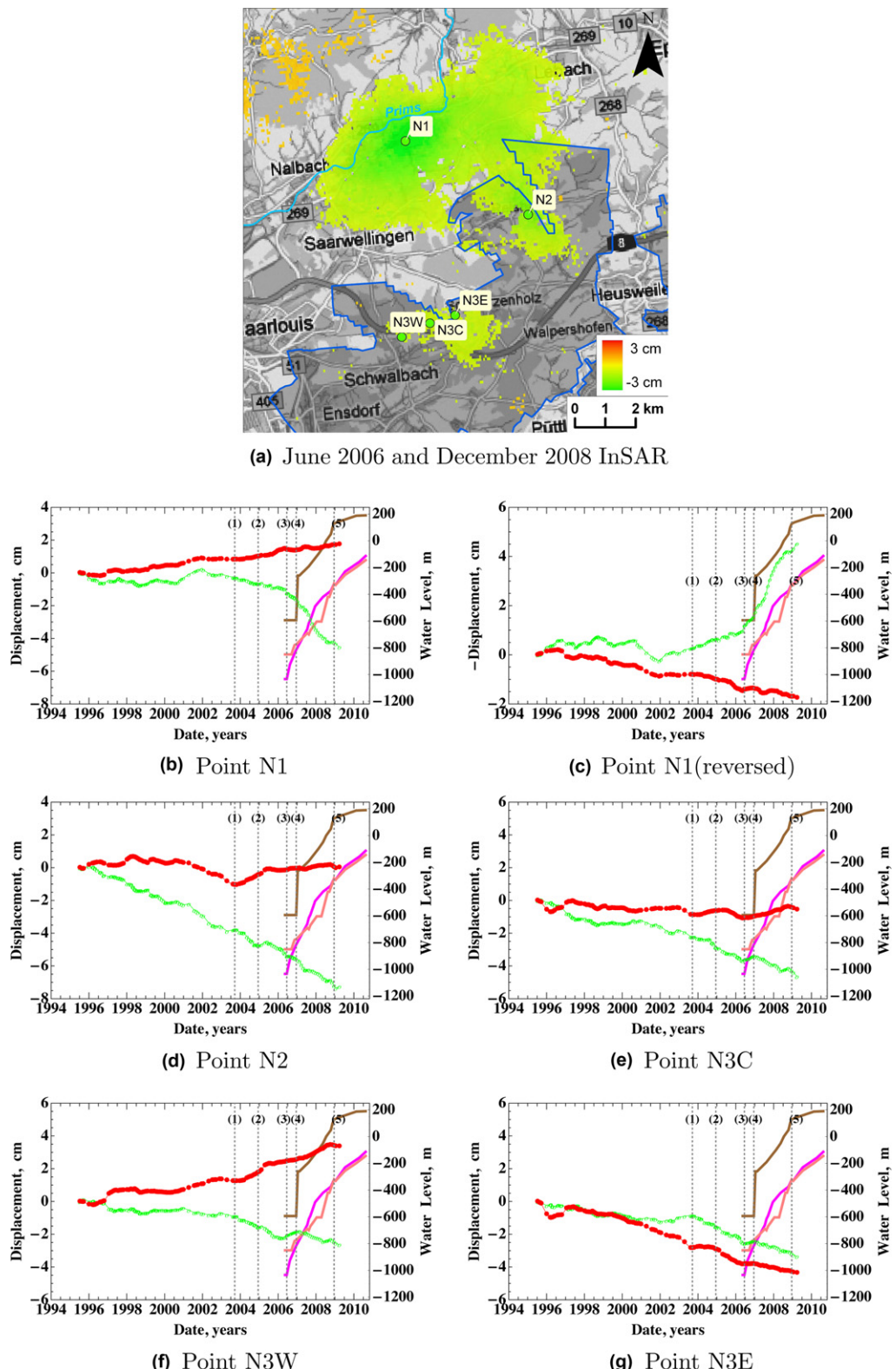


Fig. 8. (a) Ground deformation measured by proposed InSAR technique in “Northern” sector between June 2006 and December 2008. There is no leveling data available for comparison. Green dots mark N1–N3, locations of pixels for which time series are shown. (b–g) Time series of vertical (green) and east–west (red) displacements measured by proposed technique during 1995–2009 at pixels N1, N2, N3C, N3W and N3E. (c) is similar to (b) but with vertical axes reversed for easier identification of possible link with water level variations. Water levels measured in nearest pits are shown for comparison: “La Houves” (brown) and “Vouters” (magenta) in France and “Geislautern” (pink) in Germany. Scale, outlines and vertical lines are as in Fig. 5.

Points C1–C4 ([Fig. 6\(e\)–\(h\)](#)) show uplift of 3.4 cm, 2.7 cm, 0.7 cm, 1.8 cm correspondingly. The dates of BRGM leveling campaigns are tagged by the two vertical plain lines (June 2006 and December 2008). Water levels measured in the Vouters and Ludweiler pits are also plotted for comparison.

The magnitude of the vertical displacements measured at points C1 and C2 is consistent with the leveling results. Moreover, time series of point C1 ([Fig. 6\(e\)](#)) show that the subsidence did not slow after the end of exploitation (marked by the vertical dashed line (1)). Instead it started to stabilize soon after the beginning of the flooding in that sector (marked by the vertical dashed line (3)) and subsidence reversed to uplift when water level rose up to about –660 m in the nearby Vouters pit (see the Magenta curve). Uplift accelerated later when water level got shallower, possibly with a combined effect of flooding at other mining sites (see for comparison the water level measured in Ludweiler pit in black). There is almost no horizontal movement measured here as point C1 is located at the center of the subsidence but horizontal movements toward the center of deformation are visible for points located on the sides of the deforming region (not shown here). Vertical and east–west time series of displacements of pixel C2 ([Fig. 6\(f\)](#)) show a small step shortly prior the end of exploitation. Also, despite the proximity with C1, reversal from subsidence to uplift at C2 did not occur at the same time nor at the same rate. This can be attributed to the fact that flooding did not occur homogeneously over the networks and pixels C1 and C2 are located above distinct mining sites linked by galleries at unknown depths. Pixel C3 is not located directly above a mine according to the available maps, nevertheless, displacements measured by InSAR at this point seem also influenced by water levels.

In contrast, leveling results and displacements measured by InSAR disagree over the small (370 m × 650 m) area tagged C4 ([Fig. 6\(h\)](#)). Instead of the –10 cm subsidence measured by BRGM, satellite method measures a 1.6 cm uplift. However, the temporal evolution of the vertical displacement seems influenced by the flooding as for other points C1–C3 (see for instance how subsidence stabilized after the beginning of flooding marked by dashed line (1)) attesting of a reasonable measurement by InSAR.

4.2. Ground deformation in the “Western” sector

The “Western” sector includes mainly the French communes of Berviller-en-Moselle, Rémeling, Merten, Creutzwald, Ham-sous-Varsberg, Bisten-en-Lorraine, Porcelette et l'Hôpital ([Fig. 7](#)).

Leveling contour maps from BRGM flag here three distinct patches of 2 cm uplift (orange polygons in [Fig. 7\(a\)](#)) and two tiny patches of –2 cm subsidence in Bisten-en-Lorraine (green polygons in [Fig. 7\(a\)](#)). [Fig. 7\(b\)](#) shows deformation estimated by the InSAR method between the same dates (November 2006–November 2008).

Here again, space-borne measurements and leveling results are consistent although InSAR detects a broader scale subsidence above mining sites. As for the previous sector, satellite measurements do not catch the two narrow (pixel-size) subsidizing areas identified by leveling. These two patches, which are not located above a mining site, were measured along two short portions of roads located on the edge or at the base of about 50 m high hills.

[Fig. 7\(c\)–\(j\)](#) shows the details of the time series for points marked W1–W8 located in the center of the identified deforming regions mentioned here above. Water levels measured in the nearby pits are given for comparison. Deformation rate changes are clearly related to water level variations. Amplitudes of vertical deformation estimated from InSAR are slightly lower than those from leveling.

4.3. Ground deformation in the “Northern” sector

The “Northern” sector, in Germany, includes the communes of Schwalbach, Nalbach, Lebach and Saarwellingen ([Fig. 8](#)). Unlike the previous sectors mentioned above, mining activity continues here.

Although there is no water level data nor ground leveling data available for comparison, the space-borne ground deformation measurements between June 2006 and December 2008 ([Fig. 8\(a\)](#)) reveal three clearly subsidizing regions in the Northern sector: two of them are located above an active mining site (see regions tagged with pixels N2 and N3C, N3W and N3E in [Fig. 8\(a\)](#)) and one, the largest one, which is not located above any mining area (tagged with pixel N1). The large subsidence pinpointed by N1 spreads along the Prims river where more than a hundred small water ponds are located over a 2 km × 2 km area. The presence of these numerous waterbodies suggests a shallow water table or a possible discharge site for water dumped from the dewatering systems used in the nearby mines. Time series from pixel N1 ([Fig. 8\(b\)](#)) show that the subsidence started around 2004, accelerated in 2006 and decelerated at the end of 2008. Moreover, a small step visible when flooding started in the Central and Eastern sectors (vertical dashed lines (3)) suggests a possible link between that subsidence and the post-mining activity in these sectors located about 20 km away. However, unlike the deformation observed in the Western, Central and Eastern sectors, ground deformation is not directly correlated to the rise of the water level measured in the pits. Instead of an uplift, the ground is subsidizing in N1 while the water invades the flooded mines. The suggested anti-correlation between vertical ground movement and water level in La Houve, Vouters and Geislautern pits is more easily identifiable when ground displacement is inverted and plotted against the water levels as in [Fig. 8\(c\)](#). Such an anti-correlation suggest that the water that infiltrated into the galleries during the flooding may come at least partially from the water table below the Prims valley.

Sustained subsidence observed above the mining site at pixel N2 ([Fig. 8\(d\)](#)) confirms that, unlike the French mines, the ground deformation continues as neither the mining activity nor the dewatering system is stopped. Similarly the ground keeps subsidizing above the mine in the area tagged by pixels N3C, N3W and N3E ([Fig. 8\(e\) and \(f\)](#)) located respectively at the center, the western and the eastern side of the subsidizing region. Note that the pixel N3W experiences a horizontal eastward and N3E westward movements, while N2 experiences the highest rate of subsidence with no significant horizontal deformation. This is consistent with the expected deformation field in the presence of a bowl-shaped subsidence ([Samieie-Esfahany et al., 2009](#)), highlighting the ability of the proposed space-borne method to resolve the horizontal (e–w) movements.

5. Conclusions

We presented a methodology for combining ascending and descending InSAR data for calculation of two dimensional time series of ground deformation. This technique can be used for integration of an unlimited number of InSAR data sets from sensors with different acquisition parameters, such as, azimuth and incidence angles, temporal and spatial sampling and resolution, wavelength, and polarization, both air-borne and space-borne. It can also be used for computation of the 3D deformation field if data from at least three, including one non-near polar orbiting sensor (e.g. air-borne), are available.

The proposed method provides the following advantages in comparison to presently available techniques: (i) it achieves combined temporal coverage over an extended period of time when data from many different sensors with different temporal coverage

are available; (ii) it improves temporal resolution of produced time series by combining resolution from all data sets, which helps to observe a deformation signal in more detail and also improve the quality of post-processing (i.e. filtering); (iii) two or three (depending on acquisition geometry and number of available data sets) components of a ground deformation vector are computed, which helps in interpretation of observed ground deformation and further modeling and inversion; (iv) various sources of noise (i.e. tropospheric, ionospheric, topographic, orbital, thermal, etc.) are averaged out during the processing improving the signal-to-noise ratio; (v) it reduces large quantities of intermediate data (i.e. interferograms) to a single 2D or 3D product with improved characteristics, such as, signal-to-noise ratio and others mentioned above.

A few limitations were also identified. Due to rank deficiency a regularization is necessary. This can be either filtering, Tikhonov or TSVD regularization, or simple interpolation to a common temporal grid. Lack of space-borne data acquired in three independent orbital geometries limits this technique to a 2D case but such limitations can be overcome by integrating space- and airborne data together. It was also shown that spatial resolution of final products is limited to the resolution of SAR data. This issue is clearly addressed in modern sensors (e.g. RADARSAT-2 and TerraSAR-X) that are capable of delivering imagery with sub-meter resolution.

We applied the presented InSAR method for mapping ground deformation in the Greater Region of Luxembourg along the French-German border and observed ground deformation with sub-centimeter precision. We produced time series of ground deformation for twenty selected regions of interest, mainly coinciding with centers of localized subsidence. The vertical component of the time series at some locations demonstrates reversal to uplift after 2006–2007 and acceleration of subsidence at other locations. The horizontal east–west component of ground deformation shows motion toward the center of the subsidence bowl. The InSAR results were successfully compared with leveling measurements collected by the French Geological Survey (BRGM) during 2006–2008. Deformation rate changes are associated to identified water level variations measured in the mines. Due to the higher temporal and spatial resolution the proposed space-borne method detected a larger number of subsidence and uplift areas in comparison to leveling measurements restricted to annual monitoring of benchmark points along roads. We also identified deformation regions that are not precisely located above mining sites. Comparison of InSAR measurements with water levels measured in mining pits suggest that part of the water that invaded the galleries after the termination of the dewatering systems may come from these regions. The entire processing is automated and can be used for mapping ground deformation in other regions for which at least two data sets, one ascending and descending, are available. The source code is available and will be provided upon request.

Acknowledgements

ENVISAT and ERS data were provided in the frame of the European Space Agency (ESA) Cat-1 project N8548. Precise orbits were provided by the Delft Institute of Earth Observation and Space Systems (DEOS) and ESA (Cat-1 Project N7244). NRCAN/ESS contribution number is 20120317. Some maps were prepared using the Generic Mapping Tool developed by Paul Wessel and Walter H.F. Smith. Malte Helfer is thanked for sharing information about mining activity in Germany. Research by SS was in part supported by the Luxembourg National Research Fund (FNR). Research by BS was supported by the Luxembourg National Research Fund through the AFR PhD Grant N3221321.

References

- Beavan, R., Samsonov, S., Denys, P., Sutherland, R., Palmer, N., Denham, M., 2010. Oblique slip on the Puysegur subduction interface in the 2009 July Mw 7.8 Dusky Sound earthquake from GPS and InSAR observations: implications for the tectonics of southwestern New Zealand. *Geophysical Journal International* 183 (3), 1265–1286.
- Berardino, P., Fornaro, G., Lanari, R., 2002. A new algorithm for surface deformation monitoring based on small baseline differential SAR interferograms. *IEEE Transactions on Geoscience and Remote Sensing* 40 (11), 2375–2383.
- Blachowski, J., Cacon, S., Milczarek, W., 2009. Analysis of post-mining ground deformations caused by underground coal extraction in complicated geological conditions. *Acta Geodynamica et Geomaterialia* 6 (3 (155)), 351357.
- BRGM, 2009. Le bassin houiller lorrain, Surveillances 2008. <http://www.lorraine.developpement-durable.gouv.fr/groupe-d-information-sur-l-apres-a3203.html>
- Chen, F., Lin, H., Li, Z., Chen, Q., Zhou, J., 2012. Interaction between permafrost and infrastructure along the QinghaiTibet Railway detected via jointly analysis of C- and L-band small baseline SAR interferometry. *Remote Sensing of Environment* 123, 532–540.
- Costantini, M., 1998. A novel phase unwrapping method based on network programming. *IEEE Transactions on Geoscience and Remote Sensing* 36 (3), 813–821.
- Didier, C., van der Merwe, N., Betournay, M., Mainz, M., Kotyrba, A., Aydan, O., Josien, J.-P., Song, W.-K., 2008, June. Mine Closure and Post-Mining Management International State-of-the-Art. Tech. Rep. International Society for Rock Mechanics Mine Closure Commission.
- DREAL, 2008. Prévention des risques, mesures de nivellation – rapport 2008 de la direction générale de l'environnement, de laménagement et du logement de Lorraine. <http://www.lorraine.developpement-durable.gouv.fr/mesures-de-nivellation-rapport-a3213.html>
- DREAL, 2009. Prévention des risques, mesures de nivellation – rapport 2009 de la direction générale de l'environnement, de laménagement et du logement de Lorraine. <http://www.lorraine.developpement-durable.gouv.fr/mesures-de-nivellation-rapport-a3214.html>
- Farr, T., Kobrick, M., 2000. Shuttle Radar Topography Mission produces a wealth of data. *EOS Transactions, AGU* 81, 583–585.
- Ferretti, A., Prati, C., Rocca, F., 2001. Permanent scatterers in SAR interferometry. *IEEE Transactions on Geoscience and Remote Sensing* 39, 8–20.
- GIATM, 2006. Présentation de l'arrêt des exhaures. <http://www.lorraine.developpement-durable.gouv.fr/groupe-d-information-sur-l-apres-a3203.html>
- GIATM, 2007. À Porcellette. <http://www.lorraine.developpement-durable.gouv.fr/groupe-d-information-sur-l-apres-a3203.html>
- Gonzalez, P., Tiampo, K., Camacho, A., Fernandez, J., 2010. Shallow flank deformation at Cumbre Vieja volcano (Canary Islands): implications on the stability of steep-sided volcano flanks at oceanic islands. *Earth and Planetary Science Letters*.
- Hansen, C., 1987. The truncated SVD as a method for regularization. *BIT Numerical Mathematics* 27 (4), 534–553.
- Hansen, P., Jensen, S., 1998. FIR filter representation of reduced-rank noise reduction. *IEEE Transactions on Signal Processing* 46, 1737–1741.
- Hanssen, R., Feijt, A., 1996. A first quantitative evaluation of atmospheric effects on SAR interferometry. In: Proceedings of the Fringe 96 Workshop, Zurich, Switzerland.
- Hooper, A., 2008. A multi-temporal InSAR method incorporating both persistent scatterer and small baseline approaches. *Geophysical Research Letters* 35, 16302.
- Hu, J., Lib, Z., Dinga, X., Zhub, J., Sunb, Q., 2012. Spatialtemporal surface deformation of Los Angeles over 2003–2007 from weighted least squares DInSAR. *International Journal of Applied Earth Observation and Geoinformation*.
- Jiang, L., Lin, H., Ma, J., Kong, B., Wang, Y., 2011. Potential of small-baseline SAR interferometry for monitoring land subsidence related to underground coal fires: Wuda (Northern China) case study. *Remote Sensing of Environment* 115 (2), 257–268.
- Li, Z., Muller, J.-P., Cross, P., Fielding, E.J., 2005. Interferometric synthetic aperture radar (InSAR) atmospheric correction: GPS, Moderate Resolution Imaging Spectroradiometer (MODIS), and InSAR integration. *Journal of Geophysical Research* 110, (B03410).
- Massonnet, D., Feigl, K., 1998. Radar interferometry and its application to changes in the Earth surface. *Reviews of Geophysics* 36 (4), 441–500.
- Massonnet, D., Rossi, M., Carmona, C., Adragna, F., Peltzer, G., Feigl, K., 1993. The displacement field of the Landers earthquake mapped by radar interferometry. *Nature* 364, 138–142.
- Raucoules, D., Colesanti, C., Carnec, C., 2007. Use of SAR interferometry for detecting and assessing ground subsidence. *C. R. Geoscience* 339, 289302.
- Raucoules, D., Maisons, C., Carnec, C., Le Mouelic, S., King, C., Hosford, S., 2003. Monitoring of slow ground deformation by ERS radar interferometry on the Vauvert salt mine (France): Comparison with ground-based measurement. *Remote Sensing of Environment* 88 (4), 468–478.
- Rocca, F., 2003. 3D motion recovery with multi-angle and/or left right interferometry. In: Proceeding of Fringe 2003 Workshop.
- Rosen, P., Hensley, P., Joughin, I., Li, F., Madson, S., Rodriguez, E., Goldstein, R., 2000. Synthetic aperture radar interferometry. *Proceedings of the IEEE* 88 (3), 333–382.
- Samieie-Esfahany, S., Hanssen, R., van Thienen-Visser, K., Muntendam-Bos, A., 2009. On the effect of horizontal deformation on InSAR subsidence estimates. In: Proceeding of Fringe 2009 Workshop, ESA SP-677.

- Samsonov, S., Beavan, J., Gonzalez, P., Tiampo, K.J.F., 2011a. Ground deformation in the Taupo Volcanic Zone, New Zealand observed by ALOS PALSAR interferometry. *Geophysical Journal International* 187 (1), 147–160.
- Samsonov, S., d'Oreye, N., 2012. Multidimensional time series analysis of ground deformation from multiple InSAR data sets applied to Virunga Volcanic Province. *Geophysical Journal International* 191 (3), 1095–1108.
- Samsonov, S., Tiampo, K., Gonzalez, P., Manville, V., Jolly, G., 2010. Modelling deformation occurring in the city of Auckland, New Zealand mapped by the Differential Synthetic Aperture Radar. *Journal of Geophysical Research – Solid Earth* 115. (B08410).
- Samsonov, S., Tiampo, K., Rundle, J., Li, Z., 2007. Application of DInSAR-GPS optimization for derivation of fine scale surface motion maps of southern California. *IEEE Transactions on Geoscience and Remote Sensing* 45 (2), 512–521.
- Samsonov, S., van der Kooij, M., Tiampo, K., 2011b. A simultaneous inversion for deformation rates and topographic errors of DInSAR data utilizing linear least square inversion technique. *Computers and Geosciences* 37 (8), 1083–1091.
- Sandwell, D., Price, E., 1998. Phase gradient approach to stacking interferograms. *Journal of Geophysical Research* 103 (B12), 30,18330,204.
- Schmidt, D., Bürgmann, R., Nadeau, R., d'Alessio, M., 2005. Distribution of aseismic slip rate on the Hayward fault inferred from seismic and geodetic data. *Journal of Geophysical Research* 110 (B08406), 1–15.
- Small, C., 1994. A global analysis of mid-ocean ridge axial topography. *Geophysical Journal International* 116 (1), 6484.
- Strozzi, T., Delaloye, R., Poffet, D., Hansmann, J., Loew, S., 2011. Surface subsidence and uplift above a headrace tunnel in metamorphic basement rocks of the Swiss Alps as detected by satellite SAR interferometry. *Remote Sensing of Environment* 115 (6), 1353–1360.
- Tikhonov, A., Leonov, A., Yagola, A., 1998. Nonlinear Ill-Posed Problems, vol. 2. Chapman & Hall.
- Usai, S., 2003. A least squares database approach for SAR interferometric data. *IEEE Transactions on Geoscience and Remote Sensing* 41 (4), 753–760.
- Wright, T., Parsons, B., Lu, Z., 2004. Toward mapping surface deformation in three dimensions using InSAR. *Geophysical Research Letters* 31. (L01607).
- Zhang, L., Lu, Z., Ding, X., Jung, H.G.F., Lee, C., 2012. Mapping ground surface deformation using temporarily coherent point SAR interferometry: Application to Los Angeles Basin. *Remote Sensing of Environment* 117, 429–439.
- Zhao, C., Lu, Z., Zhang, Q., de la Fuente, J., 2012. Large-area landslide detection and monitoring with ALOS/PALSAR imagery data over Northern California and Southern Oregon, USA. *Remote Sensing of Environment* 124, 348–359.